



Testing the Breathing Mode in Intermediate-mass Galaxies and Its Predicted Star Formation Rate-size Anti-correlation*

Shannon G. Patel¹ , Daniel D. Kelson¹ , Nicholas Diao^{1,2}, Stephanie Tonnesen³ , and Louis E. Abramson⁴

¹ Carnegie Observatories, 813 Santa Barbara Street, Pasadena, CA 91101, USA; patel@carnegiescience.edu

² Pomona College, Claremont, CA 91711, USA

³ Center for Computational Astrophysics, Flatiron Institute, 162 5th Ave., New York, NY 10010, USA

⁴ Department of Physics & Astronomy, UCLA, 430 Portola Plaza, Los Angeles, CA 90095-1547, USA

Received 2018 July 5; revised 2018 September 26; accepted 2018 September 28; published 2018 October 15

Abstract

Recent hydrodynamical simulations predict that stellar feedback in intermediate-mass galaxies (IMGs) can drive strong fluctuations in structure (e.g., half-light radius, R_e). This process operates on timescales of only a few hundred Myr and persists even at late cosmic times. One prediction of this quasi-periodic, galactic-scale “breathing” is an *anti-correlation* between star formation rate (SFR) and R_e as central gas overdensities lead to starbursts whose feedback drags stars to larger radii while star formation dwindles. We test this prediction with a sample of 284 *isolated* IMGs with stellar masses of $10^{9.0} \leq M/M_\odot \leq 10^{9.5}$ at $0.3 < z < 0.4$ in the *Hubble Space Telescope* (*HST*) I_{814} Cosmological Evolution Survey (COSMOS) footprint. We find that IMGs with higher specific SFRs ($\text{SSFR} > 10^{-10} \text{ yr}^{-1}$) are the most extended with median sizes of $R_e \sim 2.8\text{--}3.4$ kpc and are mostly disk-dominated systems. In contrast, IMGs with lower SSFRs are a factor of $\sim 2\text{--}3$ more compact with median sizes of $R_e \sim 0.9\text{--}1.3$ kpc and have more significant bulge contributions to their light. These observed trends are opposite to the predictions for stellar feedback that operate via the “breathing” process described above. We discuss various paths to reconcile the observations and simulations, all of which likely require a different implementation of stellar feedback in IMGs that drastically changes their predicted formation history.

Key words: galaxies: evolution – galaxies: formation – galaxies: structure – galaxies: star formation

1. Introduction

Feedback from stars is predicted to play a critical role in galaxy formation, from regulating the conversion of gas into stars and shaping star formation histories (SFHs; Gerola et al. 1980; Stinson et al. 2007; Hopkins et al. 2014), to depositing metals into the circumgalactic medium and intergalactic medium via galactic winds (Larson 1974; Dekel & Silk 1986; Oppenheimer and Davé 2006), to sculpting galaxy morphologies and density profiles (Governato et al. 2010; Chan et al. 2015; El-Badry et al. 2016). These predictions are constrained by observations, such as the slope of the faint end of the galaxy stellar mass function (Cole et al. 2001; Oppenheimer et al. 2010), the detection of galactic-scale outflows among star-forming galaxies (SFGs; Rubin et al. 2014), and the presence of cored central density profiles (Marchesini et al. 2002; Simon et al. 2005; de Blok et al. 2008).

Due to limited resolution and the challenges of modeling baryonic physics, most hydrodynamical simulations implement stellar feedback using “sub-grid” prescriptions calibrated to match data (e.g., Vogelsberger et al. 2014; Schaye et al. 2015). However, the Feedback In Realistic Environments (FIRE) simulation has taken an important step by implementing explicit stellar feedback models (Hopkins et al. 2014). As a result, it may be more predictive of the evolution of galaxies across a range of halo masses. Indeed, one of FIRE’s successes is the ability to approximate various integrated observations

(e.g., stellar mass-halo mass relation) using recipes based on small scales (Hopkins et al. 2011, 2012b).

FIRE also makes predictions for the evolution in galaxy structure, which for galaxies with stellar masses of $10^7 \lesssim M/M_\odot \lesssim 10^{9.6}$ appears to be strongly coupled to star formation activity and therefore feedback (Chan et al. 2015; El-Badry et al. 2016). Specifically, in FIRE, gas cools and fuels a central starburst, which is subsequently curtailed by strong stellar feedback. As star formation subsides and the gas is expelled to large radii, it drives fluctuations in the gravitational potential, causing the stars to also migrate outward. Eventually the gas cools and falls back to the center, reversing the process and fueling another episode of concentrated star formation. This rapid, bursty cycle in FIRE (Anglés-Alcázar et al. 2017; Sparre et al. 2017) continues even at late cosmic times. One key observational prediction of this implementation of stellar feedback is that intermediate-mass galaxies (IMGs) undergo quasi-periodic fluctuations in SSFR, which is anti-correlated with half-light radius.

Here, we test that prediction against an observed sample of IMGs. Assembling such a sample is not trivial. There are only four galaxies near the Local Group spanning stellar masses $10^9 \leq M/M_\odot \leq 10^{10}$: the Large Magellanic Cloud, M33, NGC 55, and NGC 300 (McConnachie 2012). Their formation histories may be unrepresentative due to their proximity to a massive central (Andromeda or the Milky Way). For this study, we select a large sample of *isolated* IMGs from the *HST* I_{814} COSMOS footprint (Scoville et al. 2007) at $0.3 < z < 0.4$. At these redshifts, *HST* imaging affords a factor of two boost in spatial resolution (in kpc) compared to ground-based imaging at lower redshifts (e.g., the Sloan Digital Sky Survey).

* Based on observations made with the NASA/ESA *Hubble Space Telescope*, obtained at the Space Telescope Science Institute, which is operated by the Association of Universities for Research in Astronomy, Inc., under NASA contract NAS 5-26555. These observations are associated with programs 9822 and 10092.

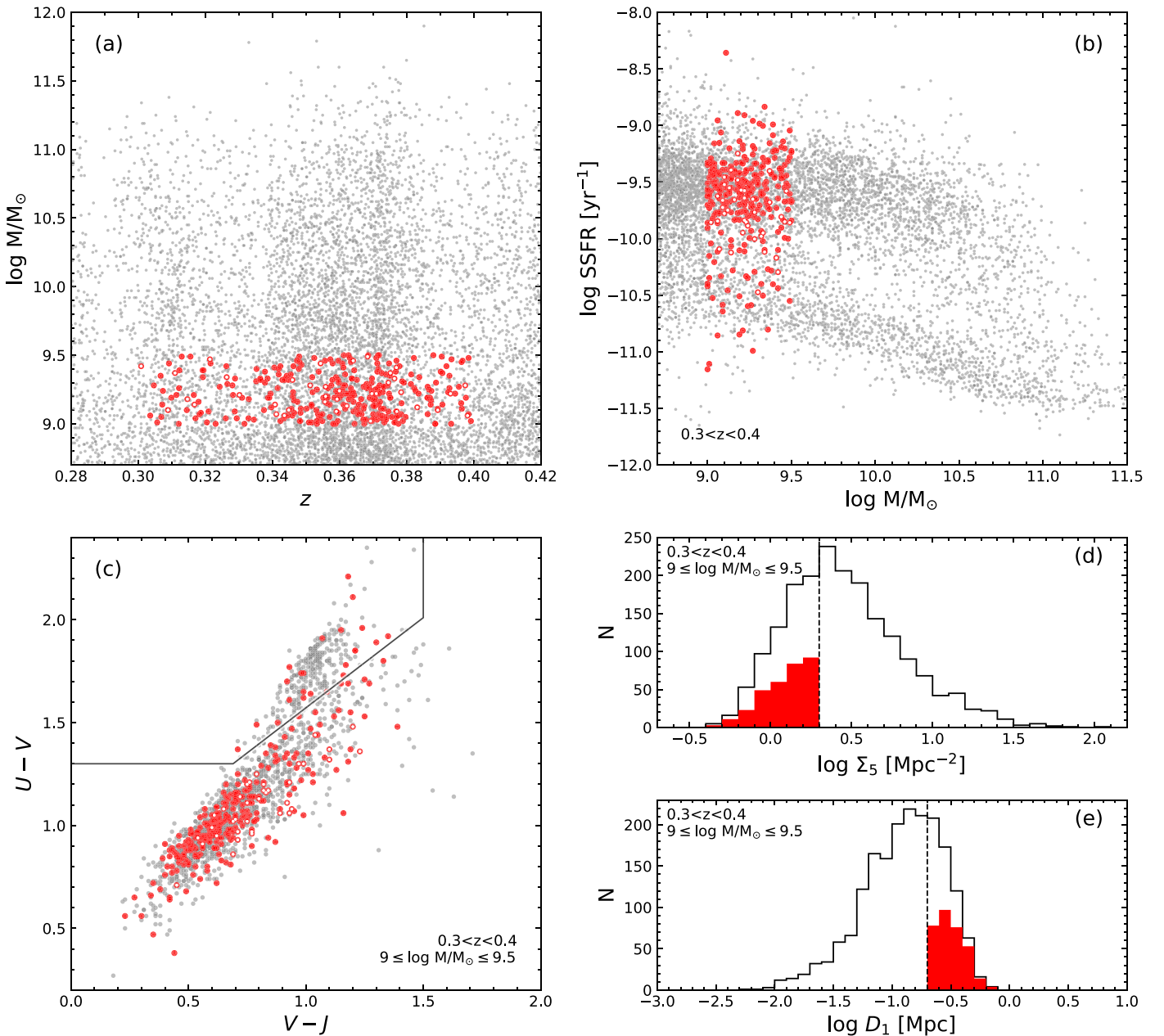


Figure 1. Selection of 284 isolated IMGs at $0.3 < z < 0.4$ with stellar mass $10^{9.0} \leq M/M_{\odot} \leq 10^{9.5}$ in COSMOS (solid red circles). (a) Stellar mass vs. redshift. (b) SSFR vs. stellar mass for galaxies at $0.3 < z < 0.4$. (c) Rest-frame $U - V$ vs. $V - J$ colors. Environmental distributions of (d) projected local galaxy density (Σ_5) and (e) distance to nearest neighbor (D_1). Isolated IMGs are defined as $\Sigma_5 < 10^{0.3} \text{ Mpc}^{-2}$ and $D_1 > 10^{-0.7} \text{ Mpc}$ (red histograms). We exclude edge-on, isolated IMGs with $b/a < 0.25$ (open red circles) from the main analysis.

We assume $H_0 = 70 \text{ km s}^{-1} \text{ Mpc}^{-1}$, $\Omega_M = 0.3$, $\Omega_{\Lambda} = 0.7$, and a Chabrier (2003) initial mass function. Magnitudes are AB.

2. Data and Analysis

We select IMGs from UltraVISTA (Muzzin et al. 2013b), which covers the *HST* ACS I_{814} footprint in COSMOS. We study IMGs at $0.3 < z < 0.4$ with stellar masses of $10^{9.0} \leq M/M_{\odot} \leq 10^{9.5}$, as these are the highest-mass galaxies for which El-Badry et al. (2016) predicted stellar feedback to significantly influence galaxy structure. A small percentage of galaxies have spectroscopic redshifts, which are used in place of photometric redshift when available. The photometric

redshift uncertainty for our sample is $\sigma_z/(1+z) \approx 0.009$, adequate for studying galaxies in different environments (e.g., Patel 2010). The stellar mass completeness limit at $z = 0.4$ is $M \sim 10^{8.7} M_{\odot}$ (Muzzin et al. 2013a)—a factor of two below the lowest masses in our sample.

We use SFRs measured by Muzzin et al. (2013b), which are derived from summing the ultraviolet (UV) and infrared (IR) flux (e.g., Bell et al. 2005). The Multiband Imaging Photometer (MIPS) $24 \mu\text{m}$ 3σ detection limit at $z = 0.4$ corresponds to $\text{SFR} \sim 0.45 M_{\odot} \text{ yr}^{-1}$. Most galaxies in the mass range studied here lack an IR detection. However, stacking the MIPS imaging at the location of spatially isolated non-detections indicates that the median IR contribution at these low masses is small ($\sim 20\%$). An analysis of lower-redshift IR-detected IMGs

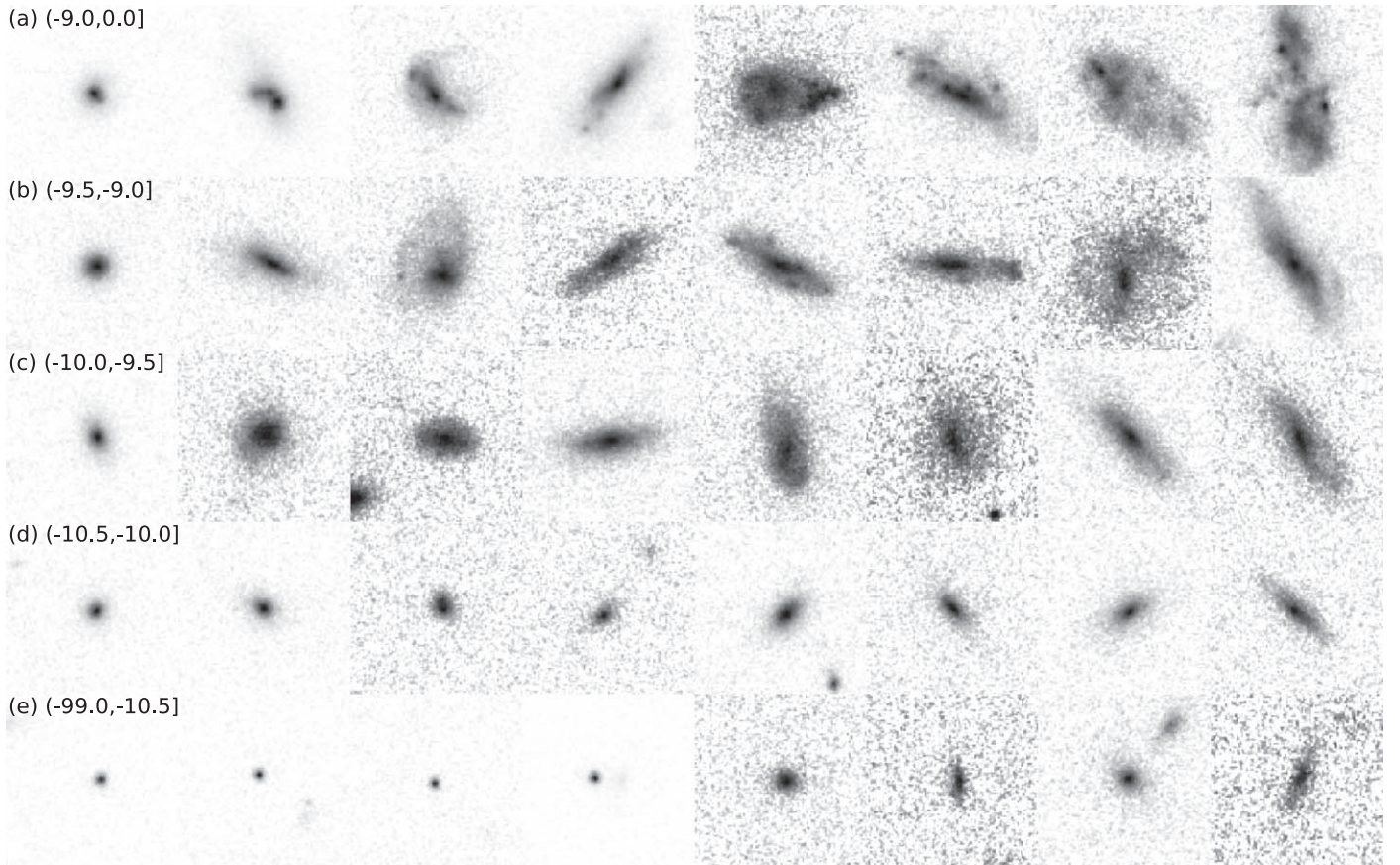


Figure 2. Example *HST* ACS I_{814} postage stamps of randomly selected, isolated IMGs with stellar mass $10^{9.0} \leq M/M_{\odot} \leq 10^{9.5}$ at $0.3 < z < 0.4$ in COSMOS. Each row is a bin in SSFR and is further sorted by half-light radius. An inverse sinh stretch is employed to reveal lower surface brightness features along with bright cores. Each stamp is $\sim 3''4$ on a side (~ 15 – 18 kpc). IMGs with higher SSFRs are typically larger in size compared to those with lower SSFRs.

confirms that the typical IR contribution to the total SFR is on this level. We take the total SFR to be the sum of the UV and IR when the latter has a $>3\sigma$ detection, otherwise the SFR is based solely on the UV.

Figure 1 shows the final IMG sample, which incorporates further cuts on environment and axis ratio (discussed below). Panel (a) shows that the redshifts are precise enough to resolve the presence of large-scale structure around $z \sim 0.37$. Panel (b) shows that while most of the IMGs lie on the SFS, their SSFRs span a wide range, from starburst to quiescent. The rest-frame $U - V$ versus $V - J$ colors in panel (c) indicate that $\sim 84\%$ of the parent IMG sample lies in the star-forming region of the diagram (e.g., Williams et al. 2009; Patel et al. 2012).

Here, we study IMGs in isolated environments so that we can compare to simulated galaxies in similar environments. We compute two different environmental measures to select galaxies, (1) in under-dense regions and, (2) isolated from any single neighbor. For (1), we compute the local galaxy density using the projected distance to the fifth nearest neighbor (Σ_5) with stellar mass $M > 10^{10.3} M_{\odot}$ and within a redshift window of $|\Delta z|/(1+z) < 0.02$. For (2), we compute the projected distance to the nearest galaxy (D_1) with stellar mass $M > 10^9 M_{\odot}$ within the same redshift window as (1). Galaxies near the survey edge with biased environmental measurements were excluded from both the parent sample and isolated subsample. Figures 1(d), (e) show the distribution of Σ_5 and D_1 . We retain galaxies with $\Sigma_5 < 10^{0.3} \text{Mpc}^{-2}$ and $D_1 > 10^{-0.7} \text{Mpc}$, resulting in 17% of the parent sample

designated as isolated (red symbols in panels a-c). The isolated sample’s *UVJ*-based SFG fraction is elevated to $\sim 93\%$ as quenched satellites are minimized by the environmental cuts.

We use the *HST* ACS I_{814} imaging in COSMOS (rest-frame *r*-band, Koekemoer et al. 2007; Scoville et al. 2007) to measure structural properties with one and two-component GALFIT Sérsic profile fits (Peng et al. 2002), incorporating similar techniques as discussed in Patel et al. (2017). The one-component fits are used to determine the half-light radii, which for our sample agree well with the literature (e.g., van der Wel et al. 2014). The two-component fits employ $n = 1$ and $n = 4$ Sérsic profiles to represent disk and bulge components, respectively, allowing us to compute bulge-to-total ratios (B/T). This quantity is an indicator of concentrated light (e.g., from a central starburst or an old spheroid). We have carried out exhaustive Monte Carlo analyses to validate the bulge-disk decompositions (S. G. Patel et al. 2019, in preparation).

Given that dust obscuration in edge-on galaxies diminishes their UV SFRs, we employ an axis-ratio cut of $b/a > 0.25$, leaving a final sample of 284 IMGs.

3. Results

Figure 2 shows example *HST* I_{814} postage stamps of the isolated IMGs. Given the redshift range, the $\sim 3''4$ postage stamps are ~ 15 – 18 kpc on a side. Each row represents a bin in SSFR, with the highest star-forming objects at the top, and the lowest on the bottom. Galaxies are further sorted by their

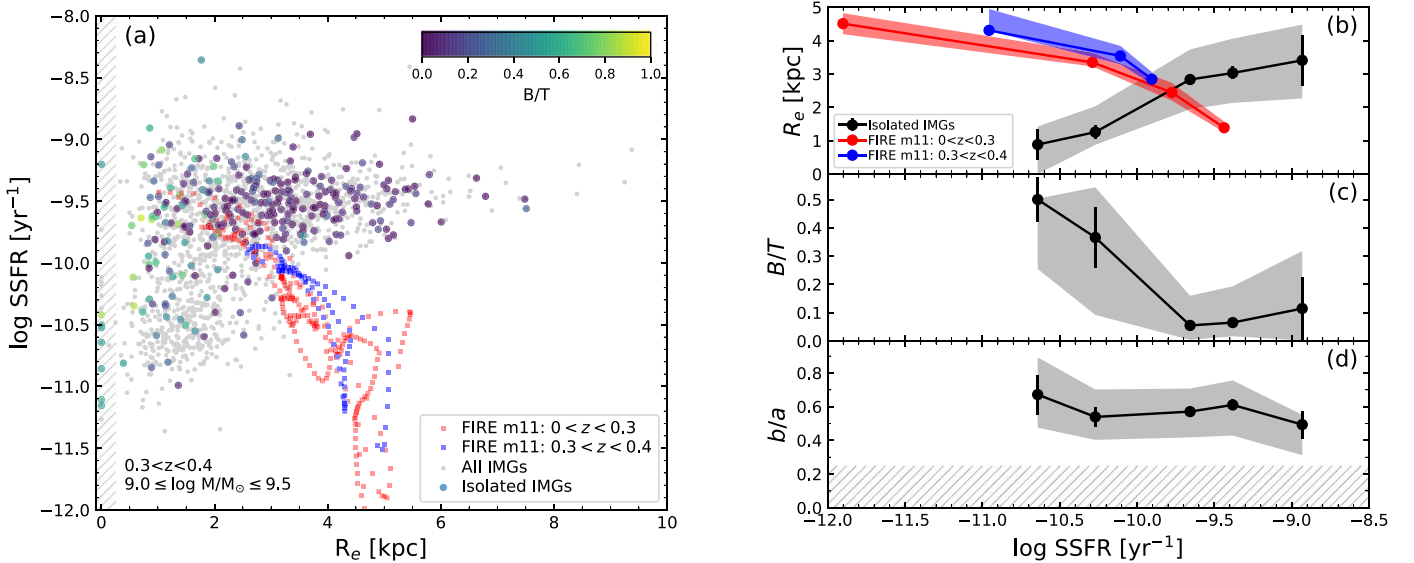


Figure 3. (a) SSFR vs. half-light radius for IMGs with stellar mass $10^{9.0} \leq M/M_\odot \leq 10^{9.5}$ at $0.3 < z < 0.4$ (gray circles). The subsample of 284 isolated IMGs are color-coded by B/T . The hatched region represents the I_{814} PSF HWHM. The squares show the evolutionary track for the simulated galaxy m11 from El-Badry et al. (2016) over $0 < z < 0.4$, sampled at timesteps of 10 Myr. The blue squares are the segment between $0.3 < z < 0.4$. Median (b) R_e , (c) B/T , and (d) b/a with 1σ bootstrapped errors in bins of SSFR for the isolated IMG sample (black) as well as m11 (blue and red; R_e only). The shaded regions indicate the interquartile range. IMGs with SSFRs above $>10^{-10} \text{ yr}^{-1}$ are generally ~ 2 – 3 times as extended as IMGs with lower SSFRs and also have lower B/T values. There is a significant offset between m11 and the observations, and more importantly, the anti-correlation between SSFR and R_e in the models conflicts with the data.

half-light radii within each SSFR bin. The difference in structure between different SSFR bins is discernible. Starbursting IMGs ($\text{SSFR} > 10^{-9} \text{ yr}^{-1}$), with stellar mass doubling times of $\lesssim 1$ Gyr (assuming sustained, constant star formation), appear somewhat diverse in their structure. Most appear to harbor disks, some are compact, and a few with several bright knots could resemble mergers but are more likely sites of intense star formation because mergers are predicted and observed to be rare in this mass range (Rodríguez-Gomez et al. 2015; Casteels et al. 2014). IMGs on the star formation sequence (SFS; $10^{-10} < \text{SSFR}/\text{yr}^{-1} < 10^{-9}$) mostly resemble extended disk-like galaxies, though a small few appear more compact and spheroidal. Below the bulk of the SFS ($\text{SSFR} < 10^{-10} \text{ yr}^{-1}$), where stellar mass doubling times exceed a Hubble time, the population is comprised predominantly of spheroids.

Figure 3 quantifies these findings and examines the connection between star formation and structure. The SSFRs for the full IMG sample are plotted against their half-light radii in gray in panel (a). The subsample of isolated IMGs are color-coded according to B/T . The median half-light radii for the different SSFR bins designated in Figure 2 are computed for isolated IMGs in panel (b). As alluded to in Figure 2, the most active star formers have the largest median size of $R_e \sim 3.4$ kpc. IMGs on the SFS have a range of sizes with a median of 2.8–3.1 kpc. Just below the SFS, the median R_e shrinks to ~ 1.3 kpc before reaching a minimum of ~ 0.9 kpc at $\text{SSFR} < 10^{-10.5} \text{ yr}^{-1}$. This trend is in agreement with the findings of Morishita et al. (2017). We note that applying a more stringent star-galaxy separation than delineated in Muzzin et al. (2013b) would remove some of the unresolved objects within the point-spread function (PSF) HWHM (hatched region in panel (a)); however, our conclusions would remain unchanged if all unresolved objects were removed.

Also shown in Figure 3 is the evolutionary track of galaxy m11 (red and blue squares) from the FIRE simulations (El-Badry et al. 2016), sampled at timesteps of 10 Myr. The $z \sim 0$

morphology of the galaxy is described by Hopkins et al. (2014) as a “fluffy dwarf spheroidal.” The displayed SFRs for this galaxy have been averaged over timescales of ~ 100 Myr, similar to the timescales probed by the UV+IR SFRs measured for our IMG sample. The half-light radius for m11 is measured in the r -band, which is the same as that employed for our sample. The simulated galaxy reaches a final mass at $z \sim 0$ of $M = 10^{9.32} M_\odot$. Tracing its SFH back to $z \sim 0.4$, this galaxy remains within the stellar mass range studied in this Letter. The rapid fluctuation in SFR causes the galaxy to oscillate between star-forming and quiescent states.

The two-component Sérsic fits reveal that the bulge component is generally more dominant among IMGs with low SSFRs (Figure 3(c)). In that regime, the bulges are likely composed of older stellar populations as opposed to a concentrated starburst. Figure 3(d) shows the median axis ratio, as well as the interquartile range ($b/a < 0.25$ omitted—hatched region). Including the edge-on systems, $\sim 43\%$ of isolated IMGs have $b/a < 0.5$. In contrast, El-Badry et al. (2016) found that none of the FIRE galaxies have axis ratios below this threshold. We note that restricting our sample to $b/a > 0.5$ does not affect our conclusions.

We identify two glaring differences in comparing the model predictions to the observations. (1) There is a substantial offset in the SSFR - R_e plane between m11 and the locus of observed isolated IMGs. (2) More importantly, the anti-correlation in the simulations between SSFR and R_e is not seen in the observations. We discuss these and other findings in the next section.

4. Discussion and Conclusions

4.1. Comparing the Simulation to the Observations

In the FIRE simulations, quasi-periodic stellar feedback is strongly coupled to fluctuations in the contemporaneous structure of present-day galaxies with stellar masses $10^7 \lesssim M/M_\odot \lesssim 10^{9.6}$, even at late times (Hopkins et al. 2014; El-Badry et al. 2016).

El-Badry et al. (2016) found that order of magnitude changes in the SFR can lead to factor of two variations in the half-light radius for the simulated galaxy, m11, over only a few hundred Myr. In fact, they argued that these variations for single galaxies reproduce the bulk of the observed scatter in the size-mass relation at fixed stellar mass. At higher masses ($M \gtrsim 10^{9.6} M_\odot$), their simulations predicted that deeper gravitational potentials are largely impervious to stellar feedback and therefore mitigate their effects, resulting in smoother SFHs. Meanwhile, at lower masses in the simulations ($M \lesssim 10^7 M_\odot$), star formation is less efficient and the resulting stellar feedback is too weak to strongly impact the gravitational potential.

Our findings in Figure 3 strongly challenge the FIRE predictions for the structural evolution of galaxies in the mass range studied here, $10^{9.0} \leq M/M_\odot \leq 10^{9.5}$. As noted in the previous section, there is a substantial offset in the SSFR- R_e parameter space spanned by the simulated galaxy, m11, and the observations. The simulated galaxy is generally too large in size given its low SFR: while m11 spends $\sim 84\%$ of its time at $0.3 < z < 0.4$ in the region with $\text{SSFR} < 10^{-10} \text{ yr}^{-1}$ and $R_e > 3 \text{ kpc}$, less than $< 1\%$ of observed IMGs are found there. In addition, most observed IMGs are SFGs, but m11 spends the vast majority of its time below the bulk of the SFS.

Even more consequential is the anti-correlation between SSFR and R_e seen in the FIRE simulations (El-Badry et al. 2016). The Pearson correlation coefficient is ~ -0.85 for m11 over $0.3 < z < 0.4$ and ~ -0.63 at $z < 0.4$. This anti-correlation forms the basis for one of FIRE’s signature predictions, as described in Section 1, of galaxies “breathing”. We do not see evidence for such a feedback loop in the observations if its presence indeed manifests in the form of an anti-correlation between SSFR and R_e . Instead, the predicted and observed SSFR- R_e distributions appear rather orthogonal. One can also compare the example *HST* images presented here to those in Figure 2 of El-Badry et al. (2016). Although the example in their figure is slightly lower mass ($M \sim 10^{8.5} M_\odot$) than the IMG sample in this work, the relative comparison is the same: at their lowest SFRs, galaxies in the simulation are extended while the data show them to be compact. Lastly, our data would also rule out a scenario where an IMG is terminally quenched by a single “breath” if the end result is an extended (e.g., $R_e \gtrsim 4 \text{ kpc}$) quiescent galaxy (QG).

4.2. Caveats

The primary caveat is that the comparison here is based on a small handful of simulated galaxies (or even a single galaxy in the case of m11). However, given that all of the FIRE galaxies with $10^7 < M/M_\odot \lesssim 10^{9.6}$ in El-Badry et al. (2016) convey a similar narrative suggests that issues arising with their evolution appear to be a fated outcome of the simulation.

It is possible that our environmental selection has not resulted in galaxies that are sufficiently isolated, but further constraining the environmental selection would shrink the sample far below the current 17% of the parent IMG sample, at which point one must ask how representative and applicable any results are for understanding general IMG formation. Moreover, it is highly unlikely that an SSFR- R_e distribution similar to that of El-Badry et al. (2016) could be extracted from the observations given the distribution of the parent population (gray circles in Figure 3). For example, employing a hypothetical environmental selection that returns 1% of the parent population (19 galaxies), and selecting random

subsamples of 19 galaxies from the parent population, results in a negative Pearson correlation coefficient between SSFR and R_e in $\sim 5\%$ of 10,000 trials and a value below < -0.50 only 0.03% of the time.

While most of our IMGs at low SSFRs ($< 10^{-10} \text{ yr}^{-1}$) lack an IR SFR component due to the MIPS detection limit, a stacking analysis at the location of the non-detections suggests low median obscured SFRs of $< 0.09 M_\odot \text{ yr}^{-1}$. This is well below the $\sim 1.6 M_\odot \text{ yr}^{-1}$ required to shift the compact galaxies at $\text{SSFR} < 10^{-10} \text{ yr}^{-1}$ to above $> 10^{-9} \text{ yr}^{-1}$ and invert the R_e -SSFR trend.

In order to determine whether the Muzzin et al. (2013b) catalog is complete for low surface brightness objects, we examined the detection rate of artificially inserted sources in the UltraVISTA K_S image (McCracken et al. 2012). We used GALFIT to generate a galaxy with an $n = 1$ Sérsic profile, $b/a = 1$, and $K_S = 22.6$. The latter was determined by taking the 90th percentile magnitude for QGs at $0.38 < z < 0.40$ around $M \approx 10^9 M_\odot$ (i.e., the faintest part of our sample). All of these values were chosen to represent the worst-case scenario in terms of detectability. We inserted the mock galaxy at 10,000 locations throughout the image and tested R_e values of 1.5, 3, 4, and 5 kpc. In regions of blank sky, we found the non-detection rate to be 0%, 2.5%, 25%, and 61%, respectively. Note that below $\text{SSFR} < 10^{-10} \text{ yr}^{-1}$ in the parent sample, there is a clearly visible decrease in the number of galaxies at $2 < R_e < 3 \text{ kpc}$. Given the high level of completeness in this region, we conclude that the drop-off at $R_e \gtrsim 2 \text{ kpc}$ is real. Furthermore, observed isolated IMGs with low SSFRs at $R_e > 3 \text{ kpc}$ are already scarce and would require a correction factor of $\gtrsim 200$ to match the duty cycle of m11 in that region (see Section 4.1), far exceeding the actual factor of ~ 1 –2 determined from our completeness simulation.

4.3. Future Directions

Our findings have several implications for numerical models of star formation and feedback. While providing a detailed account is beyond the scope of this Letter, we briefly point to several avenues for potential reconciliation with observations. (1) Hopkins et al. (2014) pointed out that while varying numerical choices (e.g., supernovae (SNe) momentum coupling) have minimal impact on key integrated quantities such as stellar masses and SFHs, they can produce significant changes to galaxy structure. (2) They also show that the nonlinear combination of multiple feedback mechanisms (e.g., H II photoionization and radiation pressure, SNe, etc.) act together to drive the strong galactic winds that are responsible for the structural variations (see also Hopkins et al. 2012a, 2012b). The degree to which these various mechanisms act in concert should therefore be explored further. (3) In general, we find that m11 exhibits low SFRs compared to the data. While this can be attributed to the galaxy lying somewhat below the KS-law (Figure 8 in Hopkins et al. 2014), addressing this issue would seemingly exacerbate the problem if stronger star formation in their simulation more strongly impacts structure. (4) El-Badry et al. (2016) found that more massive galaxies (e.g., m12i) do not exhibit a feedback loop between SSFR and R_e . Their gradual mode of star formation with less consequential stellar feedback may need to be ported to the lower masses studied here. This is supported by observations that show bursty star formation to be more pronounced in galaxies mostly below $M < 10^9 M_\odot$ (Weisz et al. 2012). (5) The observed tail of low

axis ratios suggests disks are more common at these masses than the simulations find. Maintaining rotational support is therefore critical with any feedback implementation. Collimated outflows could fulfill this requirement and are commonly found among SFGs near the IMG mass range (e.g., Chen et al. 2010; Rubin et al. 2014). Finally, we note that in FIRE-2 the qualitative behavior of galaxies in the m11 mass range remains unchanged (Hopkins et al. 2018).

In upcoming work we will explore the properties of IMGs over a wider stellar mass range and in diverse environments. The analysis will include recently obtained high signal-to-noise ratio spectroscopic observations with the Inamori-Magellan Areal Camera and Spectrograph on *Magellan*. Our aim is to understand the diversity of formation histories of IMGs beyond the four in the vicinity of the Local Group.

We thank Andrew Benson for helpful discussions.

ORCID iDs

Shannon G. Patel  <https://orcid.org/0000-0003-3350-9869>
 Daniel D. Kelson  <https://orcid.org/0000-0003-4727-4327>
 Stephanie Tonnesen  <https://orcid.org/0000-0002-8710-9206>
 Louis E. Abramson  <https://orcid.org/0000-0002-8860-1032>

References

- Anglés-Alcázar, D., Faucher-Giguère, C.-A., Kereš, D., et al. 2017, *MNRAS*, 470, 4698
- Bell, E. F., Papovich, C., Wolf, C., et al. 2005, *ApJ*, 625, 23
- Casteels, K. R. V., Conselice, C. J., Bamford, S. P., et al. 2014, *MNRAS*, 445, 1157
- Chabrier, G. 2003, *PASP*, 115, 763
- Chan, T. K., Kereš, D., Oñorbe, J., et al. 2015, *MNRAS*, 454, 2981
- Chen, Y.-M., Tremonti, C. A., Heckman, T. M., et al. 2010, *AJ*, 140, 445
- Cole, S., Norberg, P., Baugh, C. M., et al. 2001, *MNRAS*, 326, 255
- de Blok, W. J. G., Walter, F., Brinks, E., et al. 2008, *AJ*, 136, 2648
- Dekel, A., & Silk, J. 1986, *ApJ*, 303, 39
- El-Badry, K., Wetzel, A., Geha, M., et al. 2016, *ApJ*, 820, 131
- Gerola, H., Seiden, P. E., & Schulman, L. S. 1980, *ApJ*, 242, 517
- Governato, F., Brook, C., Mayer, L., et al. 2010, *Natur*, 463, 203
- Hopkins, P. F., Kereš, D., Oñorbe, J., et al. 2014, *MNRAS*, 445, 581
- Hopkins, P. F., Quataert, E., & Murray, N. 2011, *MNRAS*, 417, 950
- Hopkins, P. F., Quataert, E., & Murray, N. 2012a, *MNRAS*, 421, 3522
- Hopkins, P. F., Quataert, E., & Murray, N. 2012b, *MNRAS*, 421, 3488
- Hopkins, P. F., Wetzel, A., Kereš, D., et al. 2018, *MNRAS*, 480, 800
- Koekemoer, A. M., Aussel, H., Calzetti, D., et al. 2007, *ApJS*, 172, 196
- Larson, R. B. 1974, *MNRAS*, 169, 229
- Marchesini, D., D’Onghia, E., Chincarini, G., et al. 2002, *ApJ*, 575, 801
- McConnachie, A. W. 2012, *AJ*, 144, 4
- McCracken, H. J., Milvang-Jensen, B., Dunlop, J., et al. 2012, *A&A*, 544, A156
- Morishita, T., Abramson, L. E., Treu, T., et al. 2017, *ApJ*, 835, 254
- Muzzin, A., Marchesini, D., Stefanon, M., et al. 2013a, *ApJ*, 777, 18
- Muzzin, A., Marchesini, D., Stefanon, M., et al. 2013b, *ApJS*, 206, 8
- Oppenheimer, B. D., & Davé, R. 2006, *MNRAS*, 373, 1265
- Oppenheimer, B. D., Davé, R., Kereš, D., et al. 2010, *MNRAS*, 406, 2325
- Patel, S. 2010, PhD thesis, University of California, Santa Cruz
- Patel, S. G., Holden, B. P., Kelson, D. D., et al. 2012, *ApJL*, 748, L27
- Patel, S. G., Hong, Y. X., Quadri, R. F., Holden, B. P., & Williams, R. J. 2017, *ApJ*, 839, 127
- Peng, C. Y., Ho, L. C., Impey, C. D., & Rix, H.-W. 2002, *AJ*, 124, 266
- Rodríguez-Gomez, V., Genel, S., Vogelsberger, M., et al. 2015, *MNRAS*, 449, 49
- Rubin, K. H. R., Prochaska, J. X., Koo, D. C., et al. 2014, *ApJ*, 794, 156
- Schaye, J., Crain, R. A., Bower, R. G., et al. 2015, *MNRAS*, 446, 521
- Scoville, N., Abraham, R. G., Aussel, H., et al. 2007, *ApJS*, 172, 38
- Simon, J. D., Bolatto, A. D., Leroy, A., Blitz, L., & Gates, E. L. 2005, *ApJ*, 621, 757
- Sparre, M., Hayward, C. C., Feldmann, R., et al. 2017, *MNRAS*, 466, 88
- Stinson, G. S., Dalcanton, J. J., Quinn, T., Kaufmann, T., & Wadsley, J. 2007, *ApJ*, 667, 170
- van der Wel, A., Franx, M., van Dokkum, P. G., et al. 2014, *ApJ*, 788, 28
- Vogelsberger, M., Genel, S., Springel, V., et al. 2014, *MNRAS*, 444, 1518
- Weisz, D. R., Johnson, B. D., Johnson, L. C., et al. 2012, *ApJ*, 744, 44
- Williams, R. J., Quadri, R. F., Franx, M., van Dokkum, P., & Labbé, I. 2009, *ApJ*, 691, 1879